Int. J. Nonlinear Dynamics and Control, Vol. 1, No. 1, 2017

Nonlinear vibration signature analysis of a rotor supported ball bearings

H.K. Yadav* and D.H. Pandya

LDRP Institute of Technology and Research,
Gandhinagar – 382001, Gujarat, India
Email: himanshukyadav2@gmail.com
Email: veddhrumi@gmail.com
*Corresponding author

S.P. Harsha

Vibration Laboratory,
Mechanical and Industrial Engineering Department,
Indian Institute of Technology,
Roorkee – 247667, India
Email: spharsha@gmail.com

Abstract: The dynamic behaviour of a high speed balanced rotor supported on deep groove ball bearings (SKF-6205) has been studied by numerically simulated results. Since, internal radial clearance (IRC) is inevitably present in all class and types of bearing, in this paper it (IRC-C3) is considered as main source of nonlinearity with speed as control parameter. The complex mathematical model simulates nonlinear vibrations due to both nonlinear contact stiffness and damping at the contact of rollers and races. The contact of rollers with races are treated as nonlinear springs with contact damping whose stiffnesses are obtained by using Hertzian elastic contact deformation theory. The explicit type numerical integration technique Runge-Kutta-fourth-order method is used to solve the coupled nonlinear differential equations iteratively. Various techniques like Poincaré maps, orbits plots, and power spectra are used to study the nature of response. At lower speed transient chaos is observed which becomes stable through periodic doubling bifurcation at the medium speed. Hopf bifurcation is also observed at higher speed due to emergence of limit cycle.

Keywords: vibration signature analysis; limit cycle; Hopf bifurcation; internal radial clearance; IRC; reverses periodic flip.

Reference to this paper should be made as follows: Yadav, H.K., Pandya, D.H. and Harsha, S.P. (2017) 'Nonlinear vibration signature analysis of a rotor supported ball bearings', *Int. J. Nonlinear Dynamics and Control*, Vol. 1, No. 1, pp.1–26.

Biographical notes: H.K. Yadav received his MTech in CAD/CAM/Robotics from IIT Roorkee. His research areas are machine design, vibration, acoustics, NDT, controls and nonlinear dynamics. He has published more than six papers in various referred journals and international conference.

D.H. Pandya received his PhD in Vibration and Noise Control from IIT Roorkee. His research areas are machine design, vibration, acoustics, NDT, controls and nonlinear dynamics. He has published more than 20 papers in various referred journals.

S.P. Harsha received his PhD in Nonlinear Dynamics and Chaos from BITs Pilani and Post-Doctoral from Villanova University, Philadelphia, USA. His research areas are vibrations and control, nonlinear dynamics and chaos, rolling element bearings, design of experiments, fault diagnosis and prognosis, unmanned surface/air vehicles and CNT-based mass sensor. He has published more than 96 papers in various referred journals and 81 in international conference. He has contributed to explain term ‘waviness’ for rolling element bearing, which is also cited in Wikipedia, the free Encyclopedia.

1 Introduction

Rolling element bearings are one of the key components in rotating machinery, and their good condition is vital for the machine performance. Any bearing in operation will invariably fail at some point, with risk of machine breakdown as a result. Allowing a machine to break down before repairing is expensive as production time is lost and the bearing defect may propagate to other machine components which will also need to be replaced. The stiffness, rotational accuracy and vibration characteristics of a high-speed shaft are partly controlled by the ball bearings that support it. In the rotor bearing assembly supported by perfect ball bearings, the vibration spectrum is dominated by the vibrations at the natural frequency and the varying compliance frequency. The vibrations at this later frequency are called parametric vibrations.

For the particular bearing, the internal radial clearance (IRC) cannot be changed after manufacturing. Clearance in mechanical components introduces very strong nonlinearity. Clearance, which provided in the design of bearing to compensate the thermal expansion, is also a source of vibration and introduces the nonlinearity in the dynamic behaviour.

Sunnersjo (1978) studied the varying compliance vibrations theoretically and experimentally, taking inertia and damping forces into account. Fukata et al. (1985) first took up the study of varying compliance vibrations and the nonlinear dynamic response for the ball bearing supporting a balanced horizontal rotor with a constant vertical force. It is a more detailed analysis compared with Sunnersjo’s (1978) works as regimes of super-harmonic, sub-harmonic and chaotic behaviour are discovered. The studies undertaken by Day (1987) and Kim and Noah (1996) considered the effect of unbalanced force only, but not a varying compliance effect. In the present analysis, all the three effects, i.e., the unbalanced rotor, the varying compliance and the radial internal clearance are studied in addition to nonlinearity due to Hertzian contact. Harris (2001) considered two factors for structural vibrations of ball bearings, one of these is contact load from the balls, which deform the races into a polyhedral shape, and the other is the motion of balls relative to the line of action of the radial load which fluctuates the rigidity of the bearing.

The varying compliance effect was studied theoretically by Perret (1950) considering a deep groove ball bearing with the elastic deformation between race and balls modelled by the Hertzian theory and no bending of races. Perret studied the bearing at the instant when the balls are arranged symmetrically around the load line, i.e., with either a ball or a ball gap directly under the load. In the intermediate cage position, however, the balls are non-symmetrically arranged which means that when loaded vertically; the centre of the inner ring will undergo a horizontal as well as vertical displacement. Meldau (1951) studied theoretically the two-dimensional motion of shaft centre. Both Perret and Meldau performed a quasi-static analysis since inertia and damping force were not taken into account.

Mevel and Guyader (1993) have developed a theoretical model of a ball bearing supporting a balanced horizontal rigid rotor, with a constant vertical radial force. This is similar to the work done by Fukata et al. (1985) but more results have been reported for parametric studies undertaken and routes to chaos traced out. Chaos in this model of bearing has been reported to come out of the sub-harmonic route and the quasi-periodic route. Datta and Farhang (1997) developed a nonlinear model for structural vibration in the rolling bearings by considering the stiffness of the individual region where the elements contact each other but in this model distributed defects are not considered. Tiwari et al. (2000) has studied the effect of radial internal clearance – the appearance of sub-harmonics and Hopf bifurcation is seen theoretically where as the shift in the peak response is also observed experimentally.

Harsha et al. (2003) analysed the nonlinear behaviour of a high speed horizontal balanced rotor supported by a ball bearing. The conclusion of this work shows that the most severe vibrations occur when the varying compliance frequency (VC) and its harmonics coincide with natural frequency. Harsha (2005a) has studied the effects of radial internal clearance and rotor speed. The appearance of periodic, sub-harmonic, chaotic and Hopf bifurcation is seen theoretically. But Harsha considered only nonlinear stiffness. He studied the effects of radial internal clearance for both balanced and unbalanced rotor speed (Harsha, 2005b, 2006a). The appearance of periodic, sub-harmonic, chaotic and Hopf bifurcation is seen theoretically. But he has considered only nonlinear stiffness. Harsha (2006b) has studied the effects of rotor speed with geometrical imperfections. The results are from a large number of numerical integrations and are mainly presented in the form of Poincaré maps and frequency spectra.

The effect of fluctuation of the speed of the rotor has been studied and from the analysis performed, it was concluded that even a minimum fluctuation of the rotor speed may result in major changes of the system dynamics, indicating that speed fluctuations of the rotor are a governing parameter for the dynamic behaviour of the system. Cao and Xiao (2008) have developed the comprehensive mathematical model for the spherical roller bearing. This paper represents that the larger the radial clearance, the higher the modal density; and the higher the response at the roller passing frequency and its super harmonics. But overall the benefit of smaller radial clearance is limited in reducing the displacements of inner race.

Upadhyay et al. (2010) developed the mathematical model for the bearing by considering the nonlinear spring along with contact damping at the ball-race contact. Effect of IRC along with unbalanced rigid rotor has been explained. Period doubling and mechanism of intermittency have been observed that lead to chaos. The outcomes illustrate the appearance of instability and chaos in the dynamic response as the speed of the rotor-bearing system is changed. Also, it has been shown by Ghafari et al. (2010) that the bearing having the clearance more than 4.5 μm has more than one equilibrium point noted as strange attractor. The system vibrates around these strange attractors randomly.

It has been reported that bearing having clearance more than 12 μm has chaotic nature at 1,000 RPM onwards.

The practical occurrences of the nonlinear phenomena such as periodic, subharmonic, chaotic and Hopf bifurcation are explained in the different books of authors (Nayfeh and Balachandran, 1995; Moon, 1987; Steven, 1994). The authors want to give more importance to all these books because a different tool to identify the nonlinear behaviour of the system has been explained very nicely with plots of experiments.

2 Problem formulation

A schematic diagram of rolling element bearing is shown in Figure 1. For investigating the structural vibration characteristics of rolling element bearing, a model of bearing assembly can be considered as a spring mass damper system. Elastic deformation between races and balls gives a nonlinear force deformation relation, which is obtained by Hertzian theory. In the mathematical modelling, the rolling element bearing is considered as spring mass damper system and rolling elements act as nonlinear contact spring as shown in Figure 2. Since, the Hertzian forces arise only when there is contact deformation, the springs are required to act only in compression. In other words, the respective spring force comes into play when the instantaneous spring length is shorter than its unstressed length, otherwise the separation between balls and the races takes place and the resultant force is set to zero. The excitation is because of the varying compliance vibrations of the bearing which arise because of the geometric and elastic characteristics of the bearing assembly varying according to the cage position.

Figure 1 The flexibility of the rolling contacts in a rolling element bearing is represented by nonlinear springs and nonlinear damping

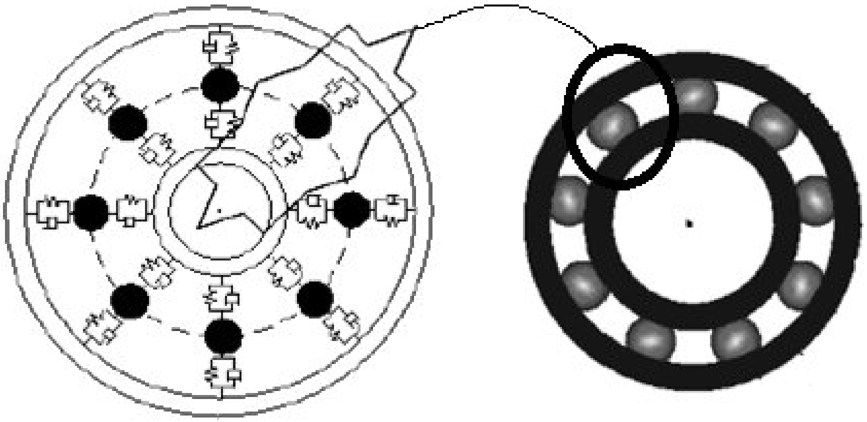

Figure 2 Mass-spring-damper of rolling element bearing (see online version for colours)

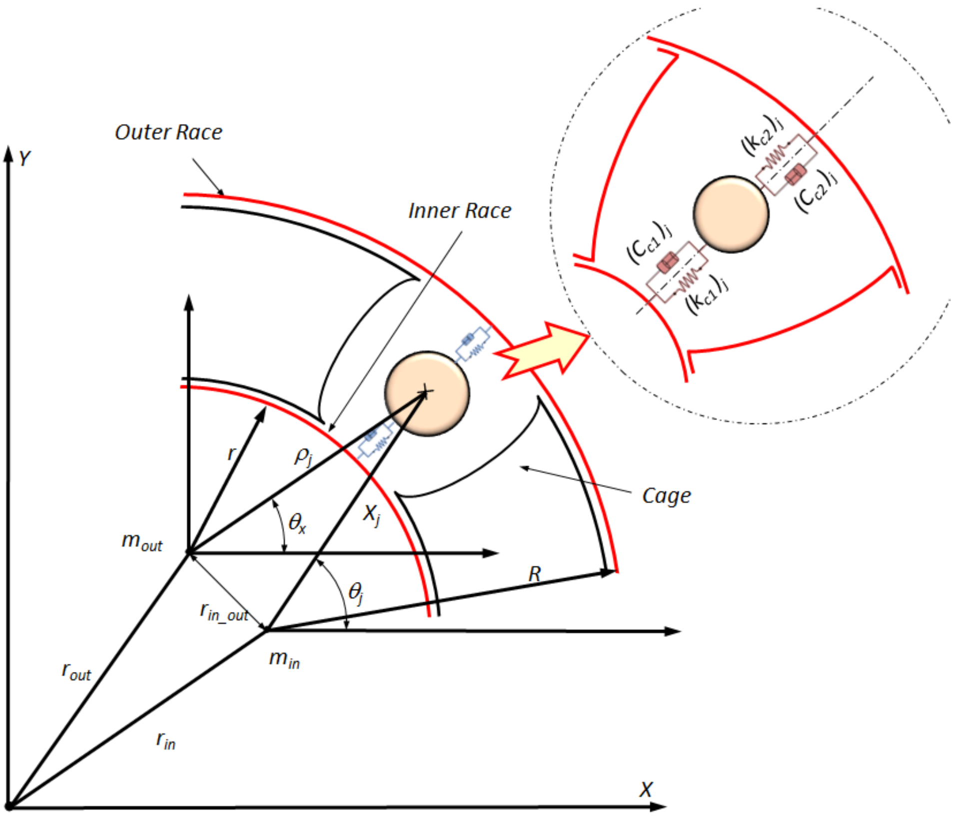

2.1 Equation of motion

The controlling equations of motion describing the dynamic behaviour of the complete model can be derived from a variational principle as Euler-Lagrange equations.

$$J = \int_0^t L dt \tag{1}$$

The equations of motion that describe the dynamic behaviour of the complete model can be derived by using Lagrange's equation for a set of independent generalised coordinates, as:

$$\frac{d}{dt}\frac{\partial T}{\partial\{\dot{p}\}} - \frac{\partial T}{\partial\{p\}} + \frac{\partial V}{\partial\{p\}} + \frac{\partial F_d}{\partial\{\dot{p}\}} = \{f\} \tag{2}$$

where T, V, p and f are kinetic energy, potential energy, vector with generalised degree-of-freedom (DOF) coordinate and vector with generalised contact forces respectively and P_d represent the dissipation energy due to damping. The kinetic and potential energies can be subdivided into the contributions from the various components i.e. from the rolling elements, the inner race, the outer race and the rotor. The kinetic energy and potential energy contributed by the inner race, outer race, balls, rotor and springs, can be differentiated with respect to the generalised coordinates ρ_j (j = 1, 2,……,N_b), x_{in}, and y_{in} to obtain the equations of motion. For the generalised coordinates ρ_j, where j = 1, 2,……,N_b, the equations are:

$$\begin{aligned}
&\ddot{\rho}_j + g\sin\theta_j + \rho_j\dot{\theta}^2 - \frac{1}{m_j}\left(k_{ir\_contact}\right)\left[\delta_{ir}\right]_+^{3/2}\frac{\partial\chi_i}{\partial\rho_i} + \frac{1}{m_j}\left(k_{or\_contact}\right)\left[\delta_{or}\right]_+^{3/2} \\
&+\frac{1}{2m_j}\frac{\partial\left[\left(k_{ir\_contact}\right)\left(\left[\delta_{ir}\right]_+^{1/2}\right)\right]}{\partial\rho_j}\left[\delta_{in}\right]_+^2 + \frac{1}{2m_j}\frac{\partial\left[\left(k_{or\_contact}\right)\left[\delta_{or}\right]_+^{1/2}\right]}{\partial\rho_j}\left[\delta_{or}\right]_+^2 \\
&+\frac{3}{2m_j}\sum_{j=1}^{N_{r.e.}}\left\{C_{in}\left(\left(K_{ir\_contact}\right)\delta_{ir+}^{3/2}\right)\left(-\chi_j\right)^q\frac{\partial\dot{\chi}_j}{\partial\dot{\rho}_j}\right\} \\
&+\frac{3}{m_j}\sum_{j=1}^{N_{r.e.}}C_{or}\left(K_{or\_contact}\right)\delta_{or+}^{3/2}\left(-\dot{\rho}_j\right)^q = 0 \quad j = 1, 2,\ldots\ldots, N_b
\end{aligned} \tag{3}$$

For the generalised coordinate x_{in} the equation is:

$$\begin{aligned}
&\ddot{x}_{ir} - \frac{1}{m_{rotation}}\sum_{j=1}^{r.e}\left(k_{ir\_contact}\right)\left[\delta_{ir}\right]_+^{3/2}\frac{\partial\chi_j}{\partial x_{ir}} \\
&+\frac{3}{2m_{rotation}}\sum_{j=1}^{N_{r.e.}}\left\{C_{ir}\left(K_{ir\_contact}\right)\delta_{ir+}^{3/2}\left(-\dot{\chi}_j\right)^q\frac{\partial\dot{\chi}_j}{\partial\dot{x}_{ir}}\right\} = \frac{F_u\sin\left(\omega_s\ t\right)}{m_{rotation}}
\end{aligned} \tag{4}$$

For the generalised coordinate y_{in} the equation is:

$$\begin{aligned}
&\ddot{y}_{ir} + g\frac{1}{m_{rotation}}\sum_{j=1}^{N_b}\left(k_{ir\_contact}\right)\left[\delta_{ir}\right]_+^{3/2} \\
&+\frac{3}{2m_{rotation}}\sum_{j=1}^{N_{r.e.}}\left\{C_{in}\left(K_{ir\_contact}\right)\delta_{ir+}^{3/2}\left(-\dot{\chi}_j\right)^q\frac{\partial\dot{\chi}_j}{\partial\dot{y}_{ir}}\right\} = \frac{\left(W + F_u\cos\left(\omega_s\ t\right)\right)}{m_{rotation}}
\end{aligned} \tag{5}$$

$$\frac{\partial\chi_j}{\partial x_{ir}} = \frac{\left(x_{or} - x_{ir}\right) - \rho_j\cos\theta_j}{\chi_j} \tag{6}$$

$$\frac{\partial\chi_j}{\partial y_{ir}} = \frac{\left(y_{or} - y_{ir}\right) - \rho_j\sin\theta_j}{\chi_j} \tag{7}$$

$$\dot{\chi}_j = \frac{1}{\chi_j}\begin{bmatrix}\rho_j\dot{\rho}_j + \dot{\rho}_j\left\{\left(x_{or} - x_{ir}\right)\cos\theta_j + \left(y_{or} - y_{ir}\right)\sin\theta_j\right\} \\ +\rho_j\dot{\theta}_j\left\{\left(y_{or} - y_{ir}\right)\cos\theta_j + \left(x_{or} - x_{ir}\right)\sin\theta_j\right\}\end{bmatrix} \tag{8}$$

$$\frac{\partial\dot{\chi}_j}{\delta\dot{x}_{ir}} = \frac{\left(x_{ir} - x_{or}\right) - \rho_j\cos\theta_j}{\chi_j} \tag{9}$$

$$\frac{\partial\dot{\chi}_j}{\partial\dot{y}_{ir}} = \frac{\left(y_{ir} - y_{or}\right) - \rho_j\sin\theta_j}{\chi_j} \tag{10}$$

where $m_{rotation} = (m_{inner} + m_{rotor})$.

This is a system of (N_b + 2) second order, nonlinear differential equations. There is no external radial force is allowed to act on the bearing system and no external mass is attached to the outer race. The '+' sign as subscript in these equations signifies that if the expression inside the bracket is greater than zero, then the rolling element at angular location θ_j is loaded giving rise to restoring force and if the expression inside bracket is negative or zero, then the rolling element is not in the load zone, and restoring force is set to zero. For the balanced rotor condition, the unbalanced rotor force (F_u) is set to be zero.

In the present paper, the authors have written the equation of motion directly. The derivation of the equation of motion has been explained in detail in Upadhyay et al. (2009).

3 Methods of solution

The coupled nonlinear second order differential equations (3) to (5) are solved by numerical integration technique which is a time domain approach. The non-analytic nature of the stiffness term renders the system equations difficult for analytical solution.

3.1 Numerical integration

The equations of motion (3) to (5) are solved by using the explicit type numerical integration technique Runge-Kutta-fourth-order method to obtain radial displacement, velocity, and acceleration of the rolling elements. For performing numerical integration, the system equations are transformed into first order form by state variable method.

$$\begin{aligned} &z_1 = x_{ir},\, z_2 = \dot{x}_{ir},\, z_3 = y_{ir},\, z_4 = \dot{y}_{ir}, \\ &\dot{z}_1 = \dot{x}_{ir} = z_2,\, \dot{z}_2 = \ddot{x}_{ir},\, \dot{z}_3 = \dot{y}_{ir} = z_4,\, \dot{z}_4 = \ddot{y}_{ir} \end{aligned} \tag{11}$$

$$z = \begin{Bmatrix} z_1 \\ z_2 \\ z_3 \\ z_4 \end{Bmatrix} = \begin{Bmatrix} x_{ir} \\ \dot{x}_{ir} \\ y_{ir} \\ \dot{y}_{ir} \end{Bmatrix} \text{ and } z = \begin{Bmatrix} \dot{z}_1 \\ \dot{z}_2 \\ \dot{z}_3 \\ \dot{z}_4 \end{Bmatrix} = \begin{Bmatrix} z_2 \\ \dot{z}_2 \\ z_4 \\ \dot{z}_4 \end{Bmatrix} = \begin{Bmatrix} \dot{x}_{ir} \\ \ddot{x}_{ir} \\ \dot{y}_{ir} \\ \ddot{y}_{ir} \end{Bmatrix}. \tag{12}$$

So, finally following four first order differential equation cab be obtained in the form of state variable, which can be solved by first order *RK* method.

$$\dot{z}_1 = \dot{x}_{ir} \tag{13}$$

$$\begin{aligned} \dot{z}_2 = {} & \frac{1}{m_{rotation}} \sum_{j=1}^{r.e} \left(k_{ir\_contact}\right) \left[\delta_{ir}\right]_+^{3/2} \frac{\partial \chi_j}{\partial x_{ir}} \\ & - \frac{3}{2m_{rotation}} \sum_{j=1}^{N_{r.e.}} \left\{ C_{in} \left(K_{ir\_contact}\right) \delta_{ir+}^{3/2} \left(-\dot{\chi}_j\right)^q \frac{\partial \dot{\chi}_j}{\partial \dot{x}_{ir}} \right\} + \frac{F_u \sin\left(\omega_s\, t\right)}{m_{rotation}} \end{aligned} \tag{14}$$

$$\dot{z}_3 = \dot{y}_{ir} \tag{15}$$

$$\begin{aligned}\dot{z}_4 &= \frac{1}{m_{rotation}}\sum_{j=1}^{N_b}\left(k_{ir\_contact}\right)\left[\delta_{ir}\right]_{+}^{3/2}\frac{\partial\chi_j}{\partial y_{ir}} \\ &\quad -\frac{3}{2m_{rotation}}\sum_{j=1}^{N_{r.e.}}\left\{C_{in}\left(K_{ir\_contact}\right)\delta_{ir+}^{3/2}\left(-\dot{\chi}_j\right)^{q}\frac{\partial\dot{\chi}_j}{\partial\dot{y}_{ir}}\right\}+\frac{\left(W+F_u\cos\left(\omega_s\, t\right)\right)}{m_{rotation}}-g\end{aligned} \tag{16}$$

Also, replacing x_{in} and y_{in} by z_1 and z_3 respectively, we can rewrite the equations (6) to (10) as following (17) to (21). Here, it is important to note that x_{in} and y_{in} are variable because they are the generalised coordinates of inner race mass centre which is moved with shaft. While x_{out} and y_{out} are the constant because mass centre of outer race is not variable. Outer race is rigidly fixed in housing.

$$\frac{\partial\chi_j}{\partial x_{ir}}=\frac{\left(x_{or}-z_1\right)-\rho_j\cos\theta_j}{\chi_j} \tag{17}$$

$$\frac{\partial\chi_j}{\partial y_{ir}}=\frac{\left(y_{or}-z_3\right)-\rho_j\sin\theta_j}{\chi_j} \tag{18}$$

$$\dot{\chi}_j=\frac{1}{\chi_j}\begin{bmatrix}\rho_j\dot{\rho}_j+\dot{\rho}_j\left\{\left(x_{or}-z_1\right)\cos\theta_j+\left(y_{or}-z_3\right)\sin\theta_j\right\} \\ +\rho_j\dot{\theta}_j\left\{\left(y_{or}-z_3\right)\cos\theta_j+\left(x_{or}-z_1\right)\sin\theta_j\right\}\end{bmatrix} \tag{19}$$

$$\frac{\partial\dot{\chi}_j}{\partial\dot{x}_{ir}}=\frac{\left(z_1-x_{or}\right)-\rho_j\cos\theta_j}{\chi_j} \tag{20}$$

$$\frac{\partial\dot{\chi}_j}{\partial\dot{y}_{ir}}=\frac{\left(z_3-y_{or}\right)-\rho_j\sin\theta_j}{\chi_j} \tag{21}$$

3.1.1 Choice of step size and initial condition

For numerical solutions, the initial conditions and step size Δt are very important for successive and economic computational solutions. Any nonlinear system is very sensitive to initial condition and for the very small perturbation of the initial condition gives a totally different behaviour. So, improper selection of initial conditions can lead to a larger computation time or sometimes unexpected results.

The larger the time step, Δt the faster the computation time but can fail in following high frequency contents. On the other hand the time step should be small enough to achieve an adequate accuracy. Also, very small time steps can increase the truncation errors (i.e. computational noise) and requires a longer time to reach a steady state. Therefore, an optimisation should be made between them.

In addition, further analyses, such as plotting Poincaré maps, computing the Lyapunov exponent, and determining the attractor's dimension, all require an integer delay at the dominant frequency which is a function of the time increment and the BPF. The time increment for all the presented simulations is computed from the following equation that yields a time delay at the BPF (Ghafari et al., 2010):

$$\Delta t=\frac{R_o+R_i}{N_b R_i f_s}\times 10^{-3} \tag{22}$$

where R_o and R_i stand for the outer and inner ring radii, N_b is the number of rolling elements, and f_s denotes the shaft rotational frequency (Hz).

At time $t = 0$ the following assumptions are made:

1. The shaft is held at the centre of the bearing such that there is no net radial load on the shaft and all balls are assumed to have equal radial preload. All the balls are equally spaced.
2. The bearing is fault-free and the only external force is the rotor's ideally balanced weight.
3. The shaft is then given initial displacements and velocities. For fast convergence the initial displacements are set to the following values: $x_{in} = 10^{-6}$ m and $y_{in} = 10^{-6}$ m. The initial velocities are assumed to be zero
4. When $t > \Delta t$ the initial conditions have already passed and the normal procedure commences.
5. All the results are obtained, after the system passes its transient state.

3.1.2 Solution procedure

The solution procedure for coupled nonlinear differential equation is explained with the flow chart as shown in Figure 3. The programming is done in MATLAB software and different response plots are obtained.

Figure 3 Flow chart of (a) main program (b) call function (see online version for colours)

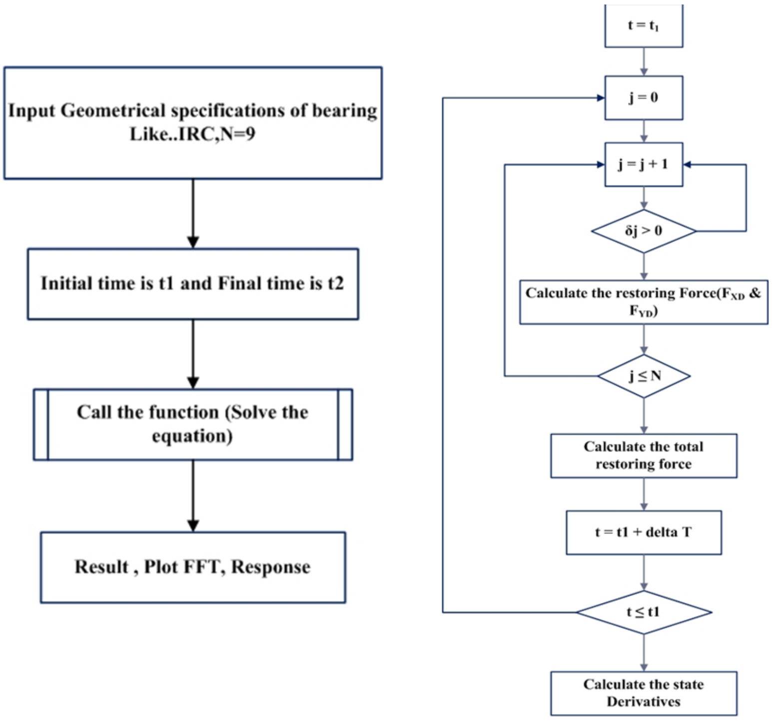

(a) (b)

3.2 Tools used for the analysis

In this paper, some qualitative tools like orbit plot, bifurcation plot, Poincaré plot and FFT plots are used to identify the dynamic nature of the system. The orbit plot is a graph in which horizontal displacement is plotted on X-axes and vertical displacement plotted on Y-axes. And, hence closed orbit of different regular or irregular shape can be observed or may be unclosed or fractal plots in case of chaos. When motion is linear periodic, the phase plane orbits traces out a circle type closed curve. But if the motion is nonlinear periodic the phase plane orbit have elliptical shape closed curve or self intersecting closed curve. If the system has higher order of period nT behaviour, then it has more number of loops in orbit or more irregular shape of closed curve. Chaotic motions have orbits that never close or repeat. Thus trajectories of the orbits in the plane will tend to fill up the section of the phase space.

In case of Poincaré map, n^{th}-order continuous time system is replaced with $(n-1)^{\text{th}}$ order map. The Poincaré map is a graph in which displacement is plotted on X-axes and velocity is plotted on Y-axes. It is constructed by sampling the phase portrait stroboscopically. Its aim is to simplify the complicated systems, and it is useful to know the nonlinear dynamic behaviour of system. Chaotic and other motions can be distinguished visually from Poincaré map. Periodic behaviour is a fixed point in Poincaré map. A quasi periodic behaviour is closed curve or points in Poincaré maps. Distinct set of points indicate the chaos in Poincaré map.

Fast Fourier transform is a plot of frequency v/s amplitude. Power spectrum is a very powerful frequency domain technique to identify the linear periodic, nonlinear periodic, superharmonics, subharmonic, quasiperiodic and different type of chaotic behaviour. If a system have undamped, unforced linear periodic type behaviour then FFT shows only a one peak of fundamental frequency of constant amplitude. While the frequency spectrum of undamped, unforced nonlinear periodic system shows peak of constant amplitude at fundamental frequency and multiples of fundamental frequency. While in case of damped, unforced linear and nonlinear periodic system the amplitudes have decreasing nature. Multiple of fundamental frequency ($n*ff$, where n is greater than 1) indicates the superharmonics nature of system. While n is less than 1 show subharmonic routes to chaos. Presence of two or more than two fundamental frequencies along with their modulation suggests the quasiperiodic nature if their ratio is incommensurate. If ratio is commensurate then the system is periodic in nature on torus. The system is said to be k^{th} -order periodic, where k is a total no. of fundamental frequency in power spectrum. It means, system having three fundamental frequencies is known as third order periodic system. The Aperiodic (chaotic) behaviour in a dynamical system is characterised by broadband frequency spectra. In addition to that, the frequency spectrum is very dense and more number of peaks can be observed around the fundamental frequency.

4 Results and discussion

To get the satisfactory post transient steady state condition, numerical simulation is run for 2 sec. To save the computational time, artificial damping, c = 50 N-s/m is used. In the present study, DGB bearing SKF 6205, class 3 type is used, in which IRC is 14 μm. The other geometrical and physical properties of bearing is listed in Table 1.

Table 1 Geometrical and physical properties of the DGB bearing SKF 6205

Bearing specification	SKF 6205
Mass of the rotor (m_r)	5 kg
Radius of inner race with point of contact with the rolling element (r)	15.56 mm
Radius of outer race with point of contact with the rolling element (R)	23.5 mm
Radius of each rolling element (ρ_r)	3.965 mm
Radial load (W)	50 N
Outside diameter	52 mm
Number of rolling elements (N_b)	9
Angular separation between elements ($\beta = 2\pi / N_b$)	40 deg
Bearing clearance (μm)	28

In the present paper, weight of balanced rigid rotor (50 N) is taken as constant radial load (W) and different types of nonlinear behaviour is identified for the speed range of 1,000 RPM to 10,000 RPM. Results of simulation of this study like Poincaré map, power spectrum and orbit plot for horizontal and vertical displacement are shown in Figures 5 to 15. As the speed is changing, the dynamical behaviour of the system is changed and that is listed in Table 2. From this study, it has been observed that at 9,000 RPM there is an occurrence of chaos through Hopf bifurcation.

Table 2 Behaviour of the system for the speed as control parameter

RPM	*Behaviour of the system*
1,000	Transient chaos-MULTIPERIODIC
2,000	Period 4T-nonlinear periodic
3,000	Period 3T-nonlinear periodic
4,000	Period 2T-nonlinear periodic
5,000	Period 2T-nonlinear periodic
6,000	Period 1T-nonlinear periodic (emergence of limit cycle)
7,000	Period 1T-nonlinear periodic (limit cycle)
8,000	Period 2T-nonlinear periodic
9,000	Chaos through Hopf bifurcation
10,000	Period 1T-nonlinear periodic (emergence of limit cycle)

Now, during the simulation it is observed that vertical displacement takes more time (2.5 sec to 5 sec) as compared to horizontal displacement (2 sec to 4 sec) to die out. Also, it is important to note that peak to peak displacement in vertical displacement is less as compared to horizontal displacement as shown in bifurcation plot (Figure 4). This fact is also reported by Harsha et al. (2003) and Tiwari et al. (2000). Also, vertical motion has a very broad band and dense frequency spectrum between VC and its multiple spikes as compared to horizontal motion. It means that, the system has more variation in vertical direction which is also conclude by Fukata et al. (1985), Harsha et al. (2003) and Tiwari et al. (2000). So, based on this discussion, the final behaviour of the system is decided almost by considering the vertical motion. In the next paragraphs, different plots are discussed in detail.

Figure 4 Bifurcation plot (peak to peak displacement response v/s speed)

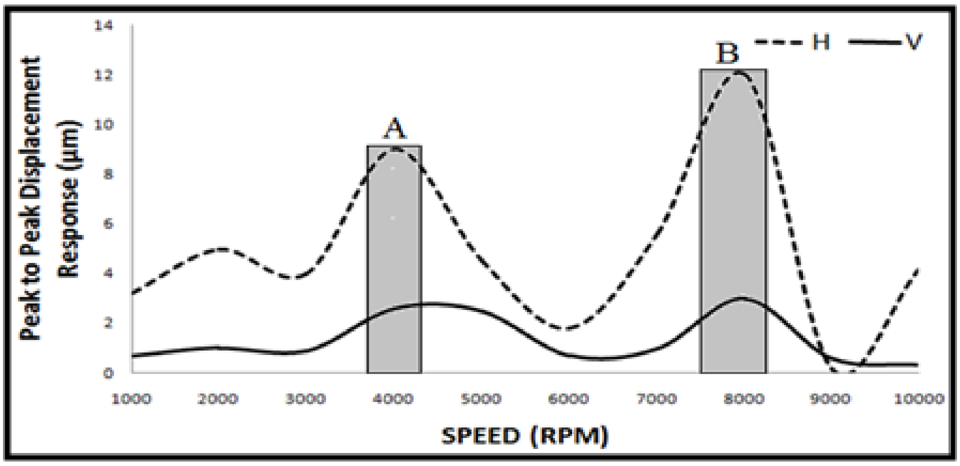

Figures 5(a) and 5(c) show Poincaré map and power spectra for horizontal displacement at the speed of 1,000 RPM respectively. Similarly, Figures 5(b) and 5(d) show Poincaré map and power spectra for vertical displacement at the speed of 1,000 RPM respectively. Two loops in Figure 5(a) indicate the period 3T behaviour, while Figure 5(b) shows the multi periodic behaviour. Now, in power spectra of horizontal displacement [Figure 5(c)], different peaks of VC and its multiples spikes like 2VC, 3VC, 4VC, 5VC and 6VC can be easily observed. Similarly, in power spectra of vertical displacement [Figure 5(d)], peak of VC can be easily observed. So, from Poincaré map and power spectra it can conclude that at 1,000 RPM system has transient type chaos behaviour. Further that can be verified from orbit plot which has closed loop, irregular shape and self intersecting trajectory as shown in Figure 15(a). Here, it is very important to note that the transient chaos is a regular nonlinear periodic motion but looks like chaos because of multiple strange attractor (Moon, 1987). This transient chaos eventually settles down in regular motion (Moon, 1987) by reverse periodic flip which is as explained further in successive paragraphs. So, finally at 1,000 RPM the system has transient type chaos or multi periodic behaviour which is also reported by Ghafari et al. (2010).

Figures 6(a) and 6(c) show Poincaré map and power spectra for horizontal displacement at the speed of 2,000 RPM respectively. Similarly, Figures 6(b) and 6(d) show Poincaré map and power spectra for vertical displacement at the speed of 2,000 RPM respectively. One loop in Figure 6(a) indicates the period 2T behaviour, while three loops in Figure 6(b) show the period 4T behaviour. Now, in power spectra of horizontal displacement [Figure 6(c)], different peaks of VC and its multiples spikes like 2VC, and 3VC can be easily observed. Similarly, in power spectra of vertical displacement [Figure 6(d)], peak of VC and its multiples spikes like 2VC, and 3VC can be easily observed. So, from Poincaré map and power spectra, it can conclude that at 2,000 RPM system has period 4T type multi periodic behaviour. Further that can be verified from orbit plot which has closed loop, irregular shape and self intersecting trajectory as shown in Figure 15(b). But it has less irregularities compared to orbit plot at 1,000 RPM. So, finally at 2,000 RPM the system has nonlinear multi periodic (period 4T) behaviour.

Figures 7(a) and 7(c) show Poincaré map and power spectra for horizontal displacement at the speed of 3,000 RPM respectively. Similarly, Figures 7(b) and 7(d) show Poincaré map and power spectra for vertical displacement at the speed of 3,000 RPM respectively. Closed orbit in Figure 7(a) indicates the periodic behaviour, while two loops in Figure 7(b) show the period 3T behaviour. Now, in power spectra of horizontal displacement [Figure 7(c)], different peaks of VC and its multiples spikes like 2VC, can be easily observed. Similarly, in power spectra of vertical displacement [Figure 7(d)], peak of VC and its multiples spikes like 2VC, and 3VC can be easily observed. So, from the Poincaré map and power spectra, it can conclude that at 3,000 RPM system has period 3T type periodic behaviour. Further that can be verified from orbit plot which has closed loop, irregular shape and self intersecting trajectory as shown in Figure 15(c). But it has less irregularities compared to orbit plot at 2,000 RPM. So, finally at 3,000 RPM the system has nonlinear period 3T type behaviour.

Figures 8(a) and 8(c) show Poincaré map and power spectra for horizontal displacement at the speed of 4,000 RPM respectively. Similarly, Figures 8(b) and 8(d) show Poincaré map and power spectra for vertical displacement at the speed of 4,000 RPM respectively. Closed orbit in Figure 8(a) indicates the periodic behaviour, while one loop in Figure 8(b) shows the period 2T behaviour. Now, in power spectra of horizontal displacement [Figure 8(c)], peak of VC can be easily observed. Similarly, in power spectra of vertical displacement [Figure 8(d)], peak of VC and its multiples spikes like 2VC, and 3VC can be easily observed. So, from Poincaré map and power spectra it can conclude that at 4,000 RPM system has period 2T type periodic behaviour. Further that can be verified from orbit plot which has closed loop, irregular shape and self intersecting trajectory as shown in Figure 15(d). But it has less irregularities compared to orbit plot at 3,000 RPM. So, finally at 4,000 RPM the system has nonlinear period 2T type behaviour.

Figures 9(a) and (c) show Poincaré map and power spectra for horizontal displacement at the speed of 5,000 RPM respectively. Similarly, Figures 9(b) and 9(d) shows Poincaré map and power spectra for vertical displacement at the speed of 5,000 RPM respectively. Closed orbit in Figure 9(a) indicates the periodic behaviour, while one loop in Figure 9(b) shows the period 2T behaviour. Now, in power spectra of horizontal displacement [Figure 9(c)], different peak of VC and its multiples spikes like 2VC can be easily observed. Similarly, in power spectra of vertical displacement [Figure 9(d)], peak of VC and its multiples spikes like 2VC, and 3VC can be easily observed. So, from the Poincaré map and power spectra it can conclude that at 5,000 RPM system has period 2T type periodic behaviour. Further that can be verified from orbit plot which has closed loop, irregular shape and self intersecting trajectory as shown in Figure 15(e). But it has less irregularities compared to orbit plot at 4,000 RPM. So, finally at 5,000 RPM the system has nonlinear period 2T type behaviour.

Figures 10(a) and 10(c) show Poincaré map and power spectra for horizontal displacement at the speed of 6,000 RPM respectively. Similarly, Figures 10(b) and 10(d) shows Poincaré map and power spectra for vertical displacement at the speed of 6,000 RPM respectively. Here, in both Poincaré map have closed elliptical orbit which indicates the nonlinear periodic behaviour. Now, in power spectra of horizontal displacement [Figure 10(c)], different peak of VC and its superharmonics like 2VC, and subharmonics VC/3 and 2/3VC can be easily observed. Similarly, in power spectra of vertical displacement [Figure 10(d)], peak of VC and its superharmonics like 2VC can be easily observed. So, from the Poincaré map and power spectra it can conclude that at 6,000 RPM system has nonlinear periodic behaviour. Further that can be verified from orbit plot which has elliptical type closed loop as shown in Figure 15(f). So, finally at 6,000 RPM the system has nonlinear period 1T type behaviour and that is known as limit cycle. So, now it can be conclude that the system become stable through reverse periodic flip.

Figures 11(a) and 10(c) show Poincaré map and power spectra for horizontal displacement at the speed of 7,000 RPM respectively. Similarly, Figures 11(b) and 10(d) show Poincaré map and power spectra for vertical displacement at the speed of 7,000 RPM respectively. Here, in both Poincaré map have closed elliptical orbit which indicates the nonlinear periodic behaviour. Now, in power spectra of horizontal displacement [Figure 11(c)], peak of VC can be easily observed. Similarly, in power spectra of vertical displacement [Figure 11(d)], peak of VC and its superharmonics like 2VC and its subharmonics like VC/7 and 3/5VC can be easily observed. So, from the time response and power spectra it can conclude that at 7,000 RPM system has nonlinear periodic behaviour. Further that can be verified from orbit plot which has elliptical type closed loop as shown in Figure 15(g). So, finally at 7,000 RPM the system still have nonlinear periodic type behaviour and existence of limit cycle is still continued.

Figures 12(a) and (c) show Poincaré map and power spectra for horizontal displacement at the speed of 8,000 RPM respectively. Similarly, Figures 12(b) and 12(d) show Poincaré map and power spectra for vertical displacement at the speed of 8,000 RPM respectively. Closed orbit in Figure 12(a) indicates the periodic behaviour, while one loop in Figure 12(b) shows the period 2T behaviour. Now, in power spectra of horizontal displacement [Figure 12(c)], peak of VC/2 can be easily observed. Similarly, in power spectra of vertical displacement [Figure 12(d)], peak of VC and its superharmonics like 2VC and its subharmonics like VC/2 can be easily observed. So, from the time response and power spectra it can conclude that at 8,000 RPM system has nonlinear periodic 2T type behaviour. Further that can be verified from orbit plot which has closed loop, irregular shape and self intersecting trajectory as shown in Figure 15(h). So, it has more irregularities compared to orbit plot at 7,000 RPM. So, finally at 8,000 RPM the system has nonlinear 2T type periodic behaviour.

Figures 13(a) and 13(c) show Poincaré map and power spectra for horizontal displacement at the speed of 9,000 RPM respectively. Similarly, Figures 13(b) and 13(d) show Poincaré map and power spectra for vertical displacement at the speed of 9,000 RPM respectively. Here, both the Poincaré map have very dense orbit and fractal structure if the orbit will be represented by points. So, it can be discerned that the system has a chaos type behaviour. Now, in power spectra of horizontal displacement [Figure 13(c)], peak of VC and its subharmonics like VC/2 can be easily observed. Similarly, in power spectra of vertical displacement [Figure 13(d)], peak of VC can be easily observed. Also, both the power spectrum has very broad band and dense frequency spectrum which indicates the chaos in system. Also, in power spectrum of horizontal displacement, subharmonic peak VC/2 has very high amplitude compared to VC and around it too many dense peaks are observed. So, from the time response and power spectra it can conclude that, at 9,000 RPM system has chaotic type behaviour. Further that can be verified from orbit plot in which orbit fills phase plane and orbit is not closed as shown in Figure 15(i). So, finally at 9,000 RPM the system has chaotic type behaviour which is happened through Hopf bifurcation. If the system becomes stable to unstable through the emergence of limit cycle oscillation or vice versa that is known as Hopf bifurcation (Moon, 1987). Since, the system has limit cycle at 7,000 RPM, period 2T at 8,000 RPM and at 9,000 RPM chaotic behaviour and again at 10,000 RPM it has limit cycle, so it can be concluded as Hopf bifurcation.

Figure 5 Response plots at 1,000 RPM, (a) Poincaré map for horizontal displacement (b) Poincaré map for vertical displacement (c) FFT for horizontal displacement (d) FFT for vertical displacement (see online version for colours)

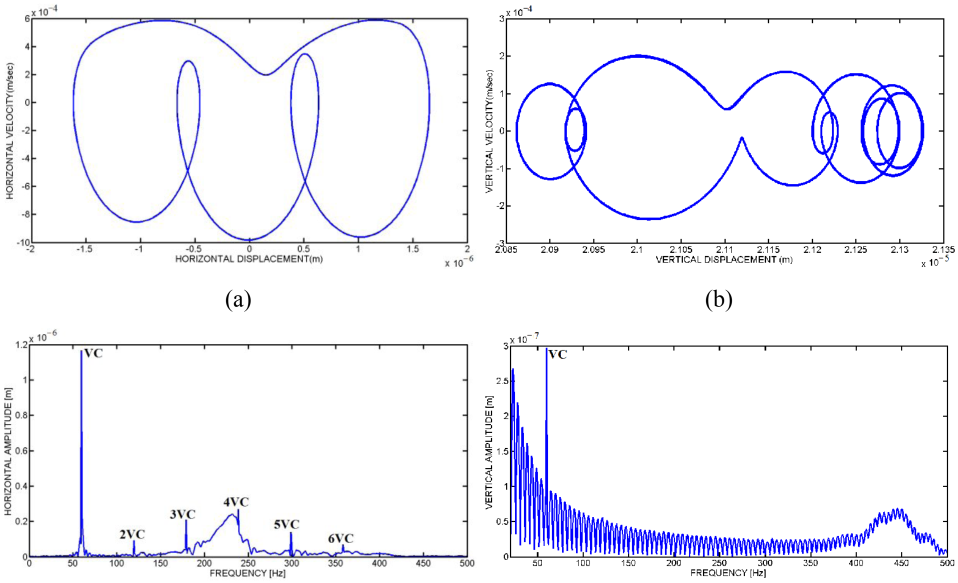

(a) (b)

(c) (d)

Figure 6 Response plots at 2,000 RPM, (a) Poincaré map for horizontal displacement (b) Poincaré map for vertical displacement (c) FFT for horizontal displacement (d) FFT for vertical displacement (see online version for colours)

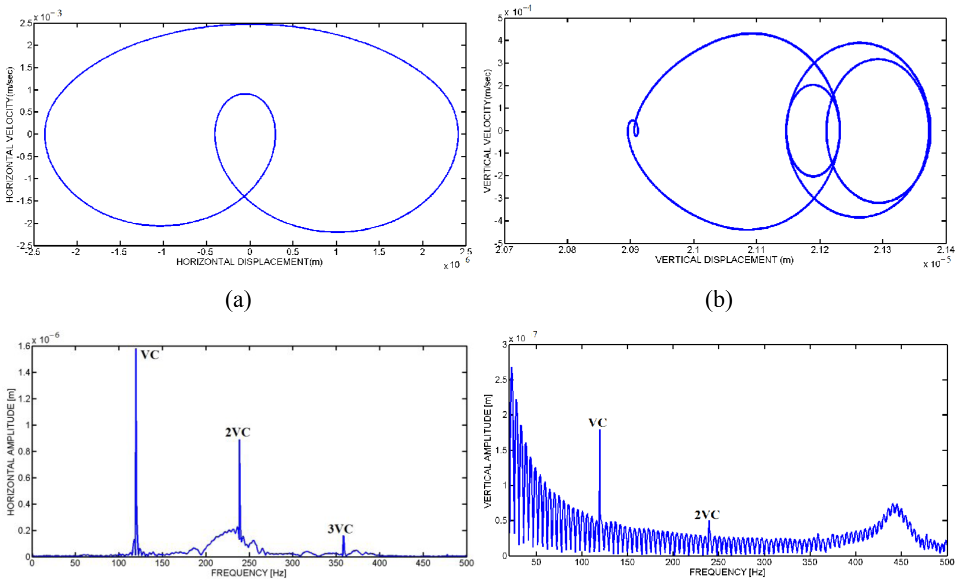

(a) (b)

(c) (d)

Figure 7 Response plots at 3,000 RPM, (a) Poincaré map for horizontal displacement (b) Poincaré map for vertical displacement (c) FFT for horizontal displacement (d) FFT for vertical displacement (see online version for colours)

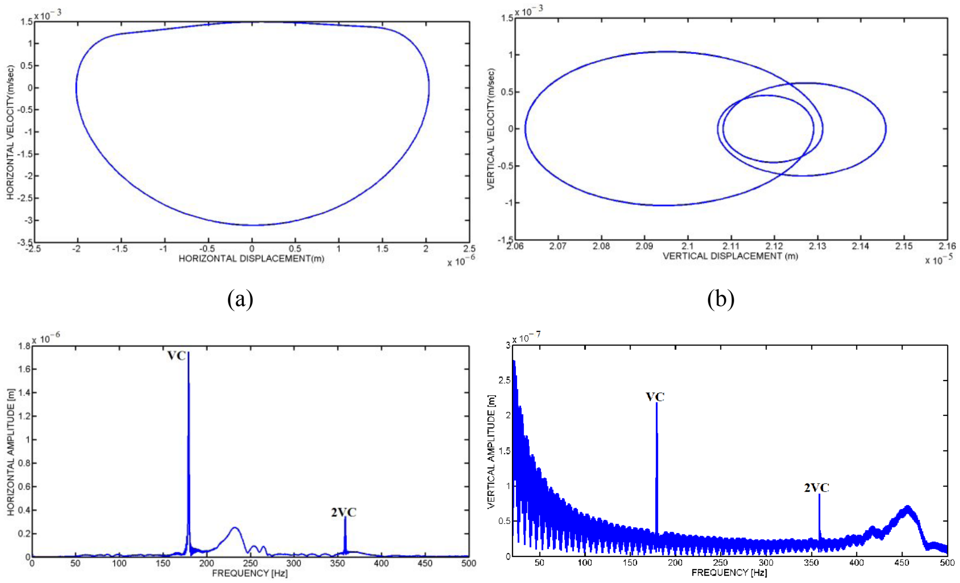

(a) (b)

(c) (d)

Figure 8 Response plots at 4,000 RPM, (a) Poincaré map for horizontal displacement (b) Poincaré map for vertical displacement (c) FFT for horizontal displacement (d) FFT for vertical displacement (see online version for colours)

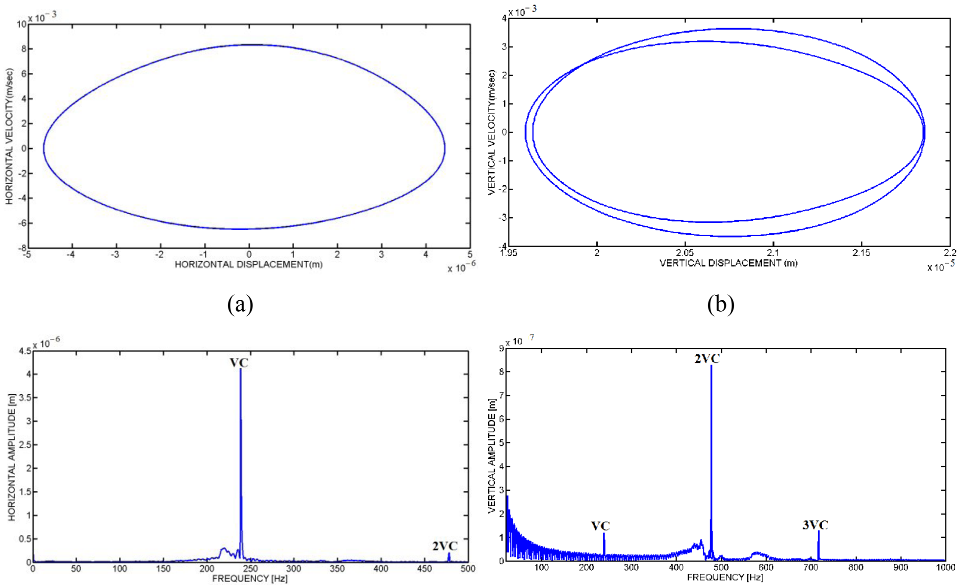

(a) (b)

(c) (d)

Figure 9 Response plots at 5,000 RPM, (a) Poincaré map for horizontal displacement (b) Poincaré map for vertical displacement (c) FFT for horizontal displacement (d) FFT for vertical displacement (see online version for colours)

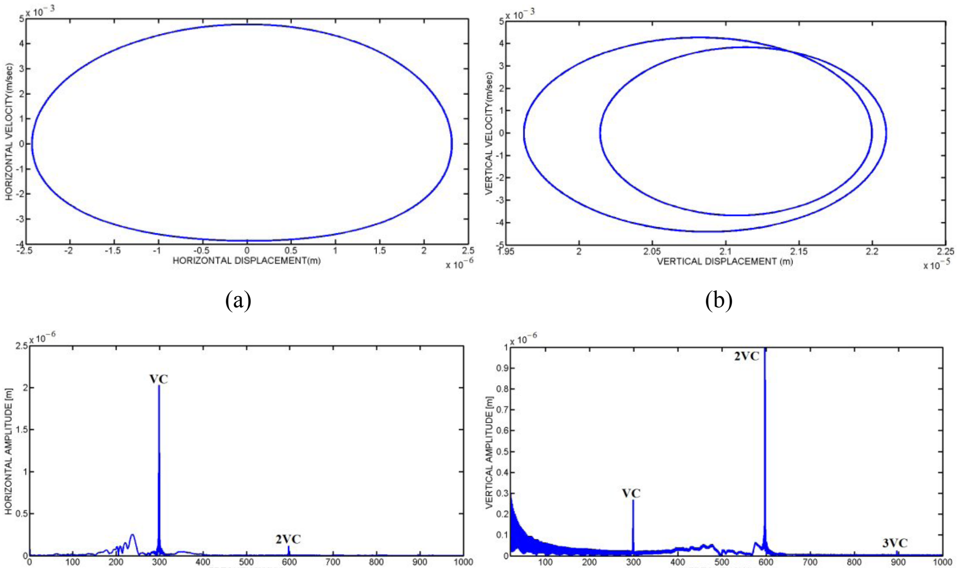

(a) (b)

(c) (d)

Figure 10 Response plots at 6,000 RPM, (a) Poincaré map for horizontal displacement (b) Poincaré map for vertical displacement (c) FFT for horizontal displacement (d) FFT for vertical displacement (see online version for colours)

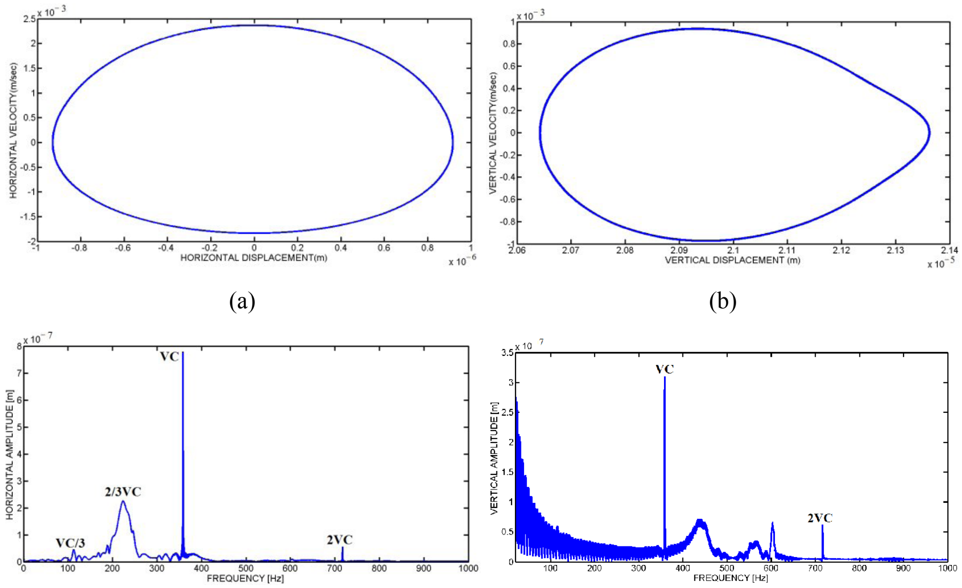

(a) (b)

(c) (d)

Figure 11 Response plots at 7,000 RPM, (a) Poincaré map for horizontal displacement (b) Poincaré map for vertical displacement (c) FFT for horizontal displacement (d) FFT for vertical displacement (see online version for colours)

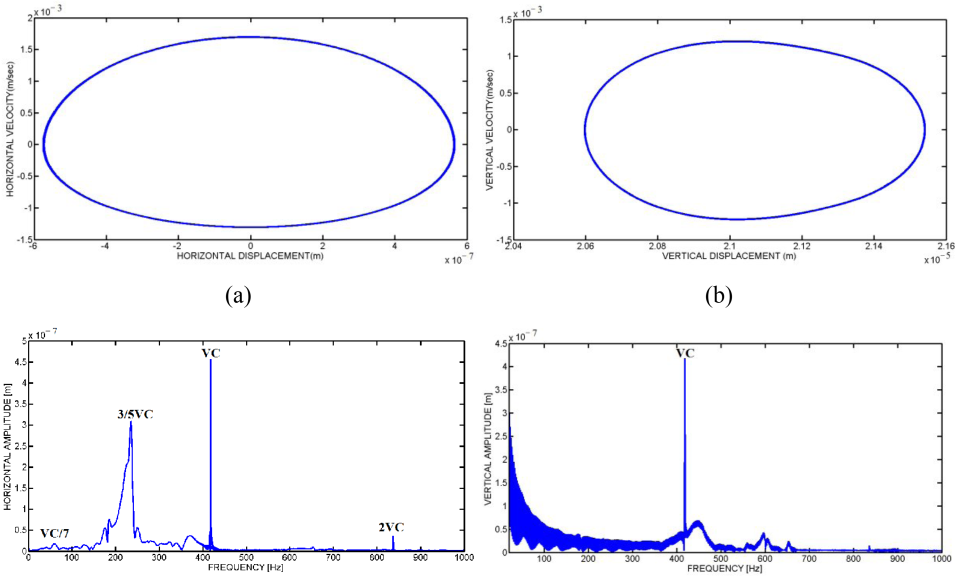

(a) (b)

(c) (d)

Figure 12 Response plots at 8,000 RPM, (a) Poincaré map for horizontal displacement (b) Poincaré map for vertical displacement (c) FFT for horizontal displacement (d) FFT for vertical displacement (see online version for colours)

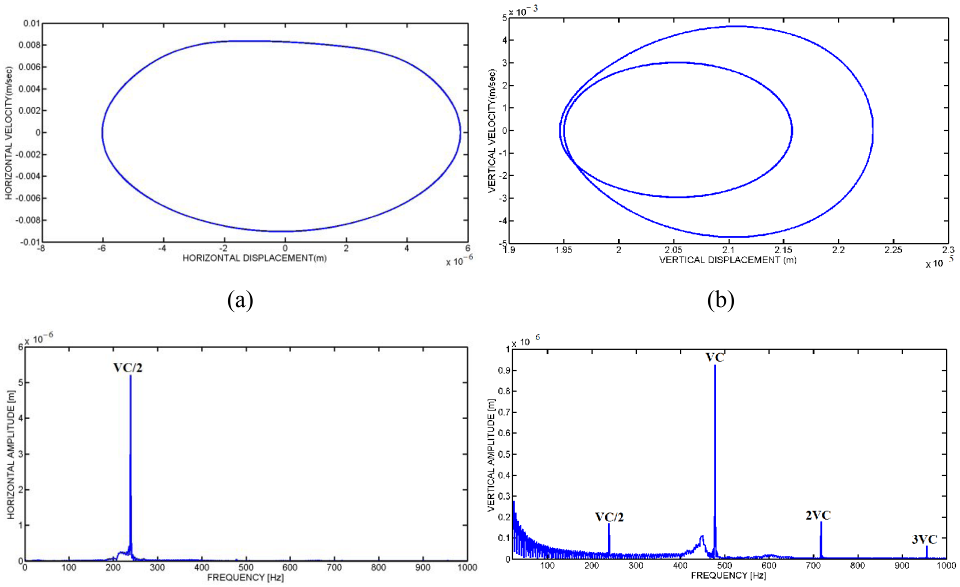

(a) (b)

(c) (d)

Figure 13 Response plots at 9,000 RPM, (a) Poincaré map for horizontal displacement (b) Poincaré map for vertical displacement (c) FFT for horizontal displacement (d) FFT for vertical displacement (see online version for colours)

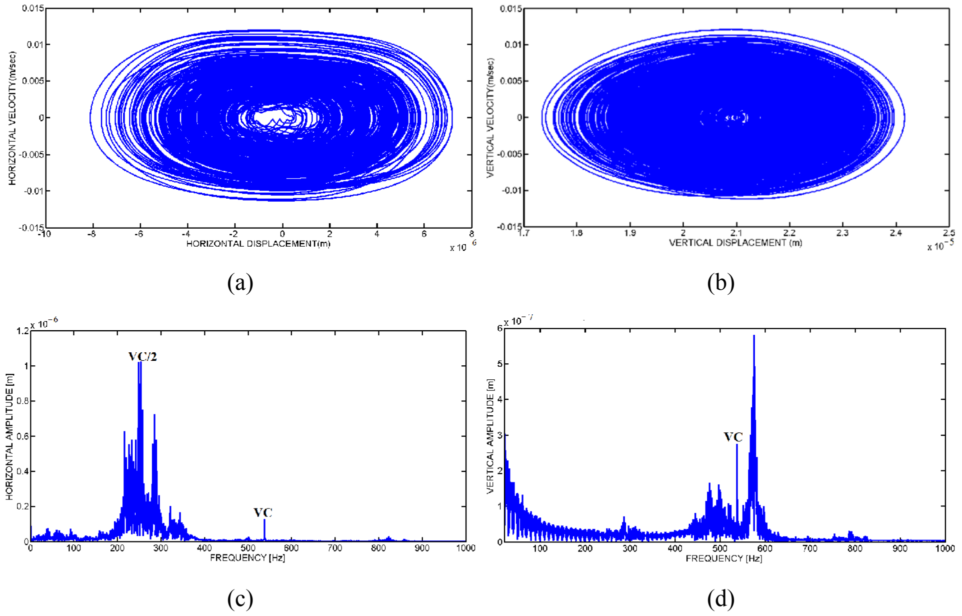

(a) (b)

(c) (d)

Figure 14 Response plots at 10,000 RPM, (a) Poincaré map for horizontal displacement (b) Poincaré map for vertical displacement (c) FFT for horizontal displacement (d) FFT for vertical displacement (see online version for colours)

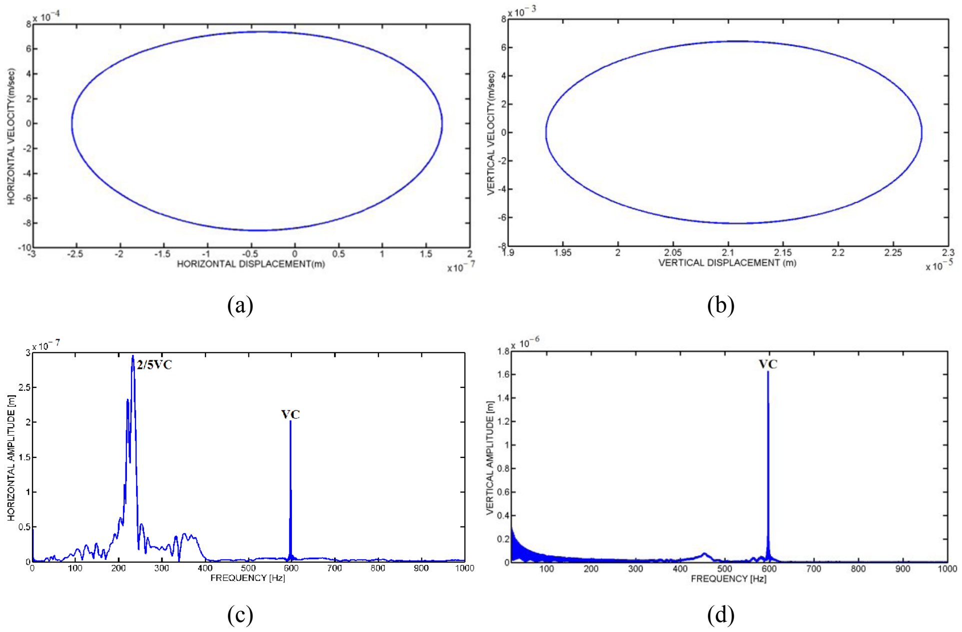

(a) (b)

(c) (d)

Figures 14(a) and (c) show Poincaré map and power spectra for horizontal displacement at the speed of 10,000 RPM respectively. Similarly, Figures 14(b) and 14(d) show Poincaré map and power spectra for vertical displacement at the speed of 10,000 RPM respectively. Here, in both Poincaré map have closed elliptical orbit which indicates the nonlinear periodic behaviour. Now, in power spectra of horizontal displacement [Figure 14(c)], peak of VC and its subharmonics 2/5VC can be easily observed. Similarly, in power spectra of vertical displacement [Figure 14(d)], only one peak of VC can be easily observed. So, from the time response and power spectra it can conclude that at 10,000 RPM system has nonlinear periodic behaviour. Further that can be verified from orbit plot which has elliptical type closed loop as shown in Figure 15(j). So, finally at 10,000 RPM there is again emergence of limit cycle which is again known as Hopf bifurcation.

Figure 15 Orbit plot for radial load W = 50 N, c = 50 N-s/m at (a) 1,000 RPM, (b) 2,000 RPM (c) 3,000 RPM, (d) 4,000 RPM, (e) 5,000 RPM, (f) 6,000 RPM, (g) 7,000 RPM (h) 8,000 RPM (i) 9,000 RPM (j) 10,000 RPM (see online version for colours)

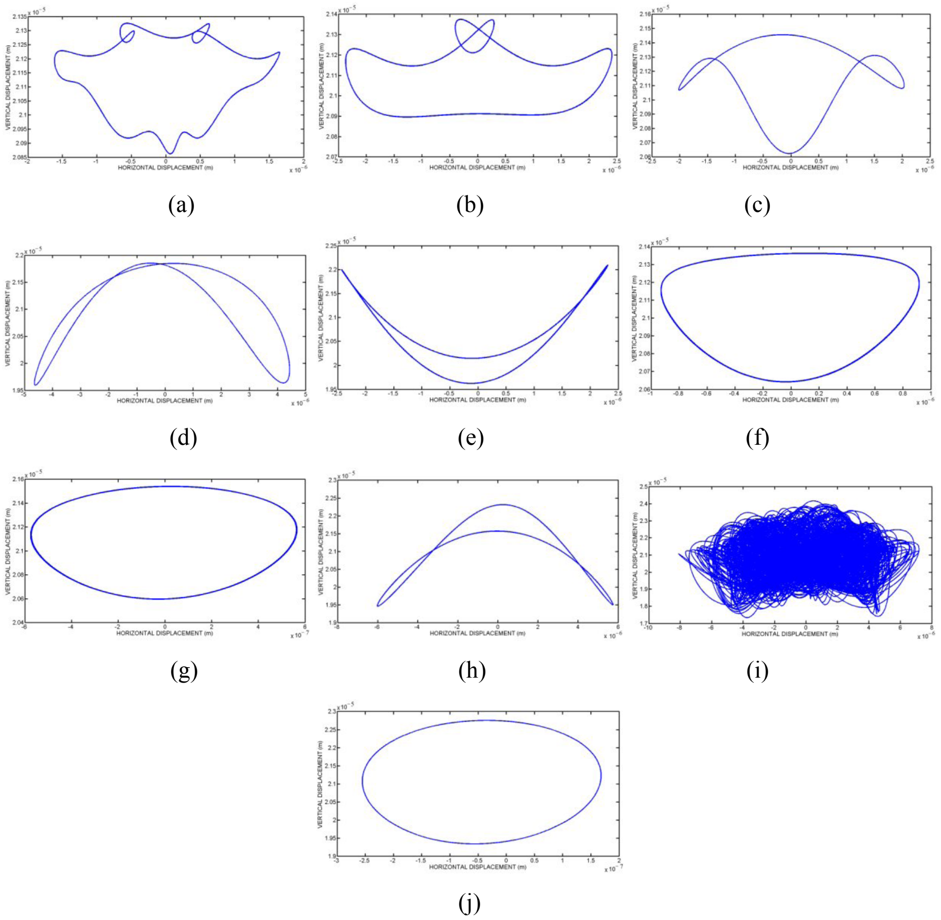

(a) (b) (c)

(d) (e) (f)

(g) (h) (i)

(j)

5 Conclusions

The sudden change in the behaviour of the system with linear change in control parameter of the system can be easily identified through bifurcation plot. Figure 4 shows the bifurcation plot for the speed as a control parameter and the difference between the peak to peak displacements of horizontal and vertical displacement is as output response. From the bifurcation plot, it can infer that the first maximum difference between the horizontal and vertical displacement is at 4,000 RPM which starts at 3,000 RPM and ends at 6,000 RPM. So, at the 4,000 RPM there is a sudden change in the behaviour of the system which starts at 3,000 RPM. And that is the system becomes stable periodic 2T type at 4,000 RPM which have previously a transient type chaotic motion at 1,000 RPM. From Table 2, it is very clear that system become periodic stable at 6,000 RPM by emergence of limit cycle through reverse periodic doubling bifurcation. As shown in bifurcation plot at the 6,000 and 7,000 RPM, the system has nonlinear periodic (1T) behaviour. The second maximum difference between the horizontal and vertical displacement is at 9,000 RPM which starts at 8,000 RPM and ends at 10,000 RPM. As discussed previously, the system has limit cycle (periodic 1T behaviour) at 7,000 RPM. While at 8,000 RPM period 2T type behaviour and at 9,000 RPM there is complete chaotic nature. And, at the 10,000 RPM there is an again emergence of limit cycle. It means before and after 9,000 RPM there is immediate immergence of limit cycle, which shows the Hopf bifurcation. So, actually it can conclude that there are two Hopf bifurcations, through one system become stable to chaotic and through the other system again become chaotic to stable.

Further, existence of superharmonics (listed in Tables 3 and 4) power spectra indicates the multi periodic nature of the system. Number of superharmonic peaks decrease with the increase in speed in FFT, which represent reverse periodic doubling. In addition to that, subharmonic peaks of VC after 7,000 RPM in FFT indicate the change in the behaviour of the system. A major peak of subharmonic at 9,000 RPM in FFT is a clear indication of bifurcation. Since there is an immediate emergence of limit cycle before and after 9,000 RPM, it can conclude as Hopf bifurcation instead of subharmonic route to chaos. So, finally following points can be summarised.

1. The system has transient type chaotic nature at 1,000 RPM, stable periodic 2T behaviour at 4,000 RPM and at 6,000 RPM there is an emergence of limit cycle.

2. The system has chaos at 9,000 RPM through Hopf bifurcation. Before and after 9,000 RPM there is an existence of limit cycle.

3. In power spectrum, number of superharmonic peaks is decreased with increase in speed. While after 6,000 RPM, number of subharmonic peaks increase.

4. So, before 6,000 RPM, the effect of superharmonic vibration is dominant and between 6,000 to 10,000 RPM, effect of subharmonic vibration is dominant.

Table 3 List of major and minor peaks for horizontal displacement

Horizontal response		
RPM	*Max. peak*	*Other peaks*
1,000	VC	2VC, 3VC, 4VC, 5VC, 6VC
2,000	VC	2VC, 3VC
3,000	VC	2VC
4,000	VC	2VC
5,000	VC	2VC
6,000	VC	VC/3, 2/3VC, 2VC
7,000	VC	VC/7, 3/5VC, 2VC
8,000	VC/2	-
9,000	VC/2	VC
10,000	2/5VC	VC

Table 4 List of major and minor peaks for vertical displacement

Vertical response		
RPM	*Max. peak*	*Other peaks*
1,000	VC	-
2,000	VC	VC, 3VC
3,000	VC	VC, 3VC
4,000	2VC	VC, 3VC
5,000	2VC	VC, 3VC
6,000	VC	2VC
7,000	VC	-
8,000	VC	VC/2, 2VC, 3VC
9,000	574.7	VC
10,000	VC	-

References

Cao, M. and Xiao, A. (2008) 'A comprehensive dynamic model of double-row spherical roller bearing – model development and case studies on surface defects, preloads, and radial clearance', *Mechanical Systems and Signal Processing*, Vol. 22, pp.467–489.

Datta, J. and Farhang, K. (1997) 'A non-linear model for structural vibrations in rolling element bearings: part I – derivation of governing equations, part – II simulation and results', *ASME Journal of Tribology*, Vol. 119, No. 1, pp.126–131.

Day, W.B. (1987) 'Asymptotic expansions in non-linear rotor dynamics', *Quarterly of Applied Mathematics*, Vol. 44, No. 4, pp.779–792.

Fukata, S., Gad, E.H., Kondou, T., Ayabe, T. and Tamura, H. (1985) 'On the radial vibrations of ball bearings (computer simulation)', *Bulletin of the Japan Society of Mechanical Engineers*, Vol. 28, No. 239, pp.899–904.

Ghafari, S.H., Abdel-Rahman, E.M., Golnaraghi, F. and Ismail, F. (2010) 'Vibrations of balanced fault-free bearings', *Journal of Sound and Vibration*, Vol. 329, No. 9, pp.1332–1347.

Harris, T.A. (2001) *Rolling Bearing Analysis*, Wiley, New York.

Harsha, S.P. (2005a) 'Non-linear dynamic response of a balanced rotor supported on rolling element bearings', *Mechanical Systems and Signal Processing*, Vol. 19, No. 3, pp.551–578.

Harsha, S.P. (2005b) 'Non-linear dynamic analysis of an unbalanced rotor supported by roller bearings', *Chaos, Solutions & Fractals*, Vol. 26, No. 1, pp.47–66.

Harsha, S.P. (2006a) 'Non-linear dynamic responses of a balanced rotor supported by rolling element bearings due to radial internal clearance effect', *Mechanism and Machine Theory*, Vol. 41, No. 6, pp.688–706.

Harsha, S.P. (2006b) 'Nonlinear dynamic analysis of high-speed rotor supported by rolling element bearings', *Journal of Sound and Vibration*, Vol. 290, No. 1, pp.65–100.

Harsha, S.P., Sandeep, K. and Prakash, R. (2003) 'The effect of speed of balanced rotor on nonlinear vibrations associated with ball bearings', *International Journal of Mechanical Sciences*, Vol. 47, No. 4, pp.225–240.

Kim, Y.B. and Noah, S.T. (1996) 'Quasi periodic response and stability analysis for a non-linear Jeffcott rotor', *Journal of Sound and Vibration*, Vol. 190, No. 2, pp.239–253.

Meldau, E. (1951) 'Die Bewegung der Achse von Walzlagern bei geringen Drehzahlen', *Werkstadt und Betreib*, Vol. 7, No. S, pp.308–313.

Mevel, B. and Guyader, J.L. (1993) 'Routes to chaos in ball bearings', *Journal of Sound and Vibration*, Vol. 162, No. 3, pp.471–487.

Moon, F.C. (1987) *Chaotic Vibrations*, John Wiley & Sons, New York.

Nayfeh, A.H. and Balachandran, B. (1995) *Applied Nonlinear Dynamics Analytical, Computational, and Experimental Methods*, Wiley, New York.

Perret, H. (1950) 'Elastiche Spielschwingungen Konstant Belaster Walzlger', *Werstatt und Betrieb*, Vol. 3, pp.354–358.

Steven, H.S. (1994) *Nonlinear Dynamics and Chaos – With Applications to Physics, Biology, Chemistry and Engineering*, Perseus Books, Perseus Books Publishing, L. L.C., New York.

Sunnersjo, C.S. (1978) 'Varying compliance vibrations of rolling bearings', *Journal of Sound and Vibration*, Vol. 58, No. 3, pp.363–373.

Tiwari, M., Prakash, O. and Gupta, K. (2000) 'Effect of radial internal clearance of a ball bearing on the dynamics of a balanced, horizontal rotor', *Journal of Sound and Vibration*, Vol. 238, No. 5, pp.723–756.

Upadhyay, S.H., Harsha, S.P. and Jain, S.C. (2010) 'Analysis of nonlinear phenomena in high speed ball bearings due to radial clearance and unbalanced rotor effects', *Journal of Vibration and Control*, Vol. 16, No. 1, p.65.

Upadhyay, S.H., Jain, S.C and Harsha, S.P. (2009) 'Nonlinear vibration signature analysis of high speed rotating shaft due to ball size variations and varying number of balls', *Proceedings of the Institution of Mechanical Engineers, Part K: Journal of Multi-body Dynamics (IMechE)*, Vol. 223, pp.83–105.

Nomenclature

k_{ir}	Equivalent nonlinear contact stiffness of the roller-inner race contact
k_{or}	Equivalent nonlinear contact stiffness of the roller-outer race contact
$k_{ir\_contact}$	Contact stiffness of the roller-inner race contact
$k_{or\_contact}$	Contact stiffness of the roller-outer race contact
r_{in}	Position of mass centre of inner race

r_{out}	Position of mass centre of outer race
T	Kinetic energy of the bearing system
T_{cage}	Kinetic energy of the cage
T_{i_race}	Kinetic energy of the inner race
T_{o_race}	Kinetic energy of the outer race
$T_{r.e}$	Kinetic energy of the rolling elements
V	Potential energy of the bearing system
V_{cage}	Potential energy of the cage
V_{i_race}	Potential energy of the inner race
V_{o_race}	Potential energy of the outer race
$V_{r.e}$	Potential energy of the rolling elements
V_{spring}	Potential energy of the spring
x_{ir}, y_{ir}	Centre of inner race
x_{or}, y_{or}	Centre of outer race
δ_{ir+}	Contact deformation of the roller-inner race
δ_{or+}	Contact deformation of the roller-outer race
I	Moment of inertia of each rolling element
I_{ir}	Moment of inertia of the inner race
I_{or}	Moment of inertia of the outer race
M_{in}	Mass of the inner race, Kg
M_j	Mass of the rolling elements, Kg
M_{out}	Mass of the outer race, Kg
M_{rotor}	Mass of the rotor, Kg
N_b	Number of balls
R	Radius of outer race
R	Radius of inner race
c	Viscous damping
c_{ir}	Equivalent viscous damping factor of the roller-inner race contact
c_{or}	Equivalent viscous damping factor of the roller-outer race contact
d	Ball diameter, Mm
D	Pitch diameter of bearing, Mm
F_{di}	Total damping contact force of the i^{th} ball

$F_{d\text{-}in}$	Ball-inner race contact damping force
$F_{d\text{-}out}$	Ball-outer race contact damping force
F_u	Unbalanced rotor force, N
L	Arc length, Mm
m	Mass of the rotor, Kg
n	Waviness order
N_b	Number of balls
N_w	Number of waves per circumference
Q	Contact force, N
R	Radius of outer race, Mm
r	Radius of inner race, Mm
$r_{\theta i}$	Elastic deformation at the point of contact at inner and outer race
V_c	Translational velocity of centre of the ball
V_{in}	Translational velocity of inner race
V_{out}	Translational velocity of outer race
W	Radial load, N
X	Rotational frequency
α	Contact angle
β	Constant angular separation between rolling elements
γ_0	IRC
λ	Wave length, Mm
ω_{bp}	Ball passage frequency due to outer race waviness
ω_{bpfi}	Inner race defect frequency
ω_{bpfo}	Outer race defect frequency
ω_{bpfs}	Ball passage frequency due to ball size variation
ω_{bsf}	Ball spin frequency
ω_{cage}	Angular velocity of cage
ω_{inner}	Angular velocity of inner race
ω_{outer}	Angular velocity of outer race
ω_{roll}	Angular velocity of ball
ω_{rotor}	Angular velocity of rotor
ω_{wp}	Wave passage frequency

Π_{in}	Amplitude of the wave at inner race
Π_{out}	Amplitude of the wave at outer race
Π_m	Initial amplitude of the M^{th} sinusoidal wave at inner race
Π_n	Initial amplitude of the nth sinusoidal wave at outer race
$\Sigma\rho$	Sum of curvature of the contacting bodies
ρ_r	Radius of each rolling element, mm
θ_j	Angular position of rolling element
Δ_i	Additional deformation in the contact deformation
Δ_{in}	Additional deformation in the contact deformation due to inner race waviness
Δ_{out}	Additional deformation in the contact deformation due to outer race waviness
VC	Varying compliance frequency
Fc	Cage frequency
BPF	Ball passage frequency
BPV	Ball passage vibration
FFT	Fast Fourier transformations
WPF	Wave passage frequency.